Journal of Geophysical Research: Solid Earth

RESEARCH ARTICLE
10.1029/2017JB015002

Gravitational Potential Energy in Iberia: A Driver of Active Deformation in High-Topography Regions

M. Neres[1,2], M. C. Neves[3], S. Custódio[1], M. Palano[4], R. Fernandes[5], L. Matias[1], M. Carafa[6], and P. Terrinha[1,2]

[1]Instituto Dom Luiz, Faculdade de Ciências, Universidade de Lisboa, Lisbon, Portugal, [2]Instituto Português do Mar e da Atmosfera, Lisbon, Portugal, [3]Instituto Dom Luiz, Universidade do Algarve, Faro, Portugal, [4]Istituto Nazionale di Geofisica e Vulcanologia, Catania, Italy, [5]Instituto Dom Luiz, Universidade da Beira Interior, Covilhã, Portugal, [6]Istituto Nazionale di Geofisica e Vulcanologia, L'Aquila, Italy

Key Points:
- We present a new estimation of GPE in Iberia, which is compared to stress indicators and to a new/updated Iberian strain rate field
- GPE leads to local deviations in the main tectonic stress field in Iberia, causing extensional stress regimes over high-topography regions
- Both GPE and the long-wavelength topography of Iberia result from the propagation of plate boundary stresses into the intraplate domain

Supporting Information:
- Supporting Information S1
- Table S1

Correspondence to:
M. Neres,
neresmarta@gmail.com

Citation:
Neres, M., Neves, M. C., Custódio, S., Palano, M., Fernandes, R., Matias, L., et al. (2018). Gravitational potential energy in Iberia: A driver of active deformation in high-topography regions. *Journal of Geophysical Research: Solid Earth*, *123*. https://doi.org/10.1029/2017JB015002

Received 18 SEP 2017
Accepted 13 OCT 2018
Accepted article online 17 OCT 2018

Abstract In this study, we present a new estimation of the gravitational potential energy (GPE) in Iberia and use numerical modeling to evaluate its relative contribution to the present-day stress field and deformation. We also present an improved (larger time span and denser coverage) compilation of Global Navigation Satellite System velocities, which we use to compute the strain rate field of Iberia. We take advantage of recent neotectonic modeling developed for Iberia and northwest Africa to study the isolated dynamic contribution of GPE-related stresses. We present two models—one including only the stress generated by GPE and another reproducing the net stress field—and compare their predictions with the most up-to-date compilations of stress indicators, hypocenter clusters, and geodetic strain rates. The main effect of GPE is to induce second-order spatial variations in the stress field. GPE appears to play an important role in high-topography regions, where it explains deviatoric stress patterns mainly associated with extensional regimes. In north Iberia, especially in the Pyrenees and Cantabria, GPE causes an extensional regime over the highest peaks. In the Iberian Chain and eastern Betics, GPE is in agreement with the observed extensional deformation. Normal focal mechanisms of shallow earthquake clusters appear to be related with GPE maxima and GPE-induced extensional regimes. Wavelength analysis suggests that both GPE and the long-wavelength topography of intraplate Iberia record the plate boundary forces that acted in Iberia during the Alpine orogeny at Eocene to lower Miocene times.

1. Introduction

Lateral variations in the distribution of mass in the lithosphere give rise to horizontal gradients in gravitational body forces, which in turn give rise to horizontal lithospheric stresses. The role of these gravitational body forces in driving the dynamics and deformation of the lithosphere has gained attention in recent decades. Global studies show that long-term plate motions, stresses, the deformation of plate boundary zones, and geoid are best fit when gravitational potential energy (GPE), plate boundary, and deep mantle dynamic forces are considered (Ghosh, Holt, et al., 2013; Ghosh & Holt, 2012; Lithgow-Bertelloni & Richards, 1998). GPE may be expected to play an especially important role in intraplate and transitional slow-deforming regions, where plate boundary forces become weaker. Tectonic deformation driven by large GPE gradients in regions of varying crustal thickness, such as mountain ranges and continental margins, has been extensively demonstrated (Artyushkov, 1973; Fleitout & Froidevaux, 1982; Ghosh et al., 2006; Molnar & Lyon-Caen, 1988; Pascal & Cloetingh, 2009). In sectors of western North America (e.g., Ghosh, Becker, et al., 2013; Jones et al., 1996) and Africa (e.g., Coblentz & Sandiford, 1994; Stamps et al., 2014, 2015), numerical modeling has supported GPE as a dominant deformation-driving force. Recent studies have even suggested that body forces play a deterministic role in controlling the state of stress and also the location and style of intraplate earthquakes in central North America (Levandowski et al., 2017). Other studies attribute a more important role to the rate of change of dynamic topography (i.e., vertical normal stress of mantle flow) in driving intraplate seismicity and deformation (Becker et al., 2015; Moucha & Forte, 2011). GPE is also important at collisional plate boundaries, in association withmountain building processes (e.g., Hodges et al., 2001).

For the Eurasian plate, including its southern boundary, studies incorporating GPE, basal tractions, and plate boundary edge collision forces (Warners-Ruckstuhl et al., 2013) concluded that the large-scale Eurasian stress

field is governed by edge collision forces, rather than by tractions from mantle flow. However, models of global mantle convection (see, for instance, Faccenna & Becker, 2010; Rubey et al., 2017) argue that dynamic topography induced by mantle flow may be responsible for shaping mobile belts and for microplate motion along the southern boundary of the Eurasian plate. Neotectonic dynamic modeling by Carafa, Barba, et al. (2015) evaluated the torque balance for the Mediterranean plates and concluded that lithostatic stresses play a key role in Anatolia, whereas side (collisional) and basal strengths are the main drivers of deformation in the Adria and Aegean Sea plates.

The role of dynamic processes in generating topography or whether topography is isostatically or dynamically supported are outstanding questions in geodynamics. In a review of this topic, Molnar et al. (2015) noted that flow-induced basal tractions on the lithosphere may account for relatively small ($<$300-m) deflections of the Earth's surface and argued that isostatically compensated density contrasts associated with variations of GPE provide both qualitative and quantitative explanations of continental deformation.

The stress field of Iberia has been thoroughly modeled by Andeweg (2002). However, the role of GPE remains poorly understood, mainly due to unknowns about the lithospheric structure that limit resolution in the intraplate region. Neves et al. (2014) used new constraints on the Iberian crustal structure to reassess the role of GPE in determining intraplate stress and strain rate patterns. They presented three alternative GPE estimates: two based on distinct hypothesis of isostatic compensation to estimate the subcrustal lithospheric structure and a third one using the EGM2008 geoid model. In order to compute the stress distribution arising from body forces, Neves et al. (2014) used the thin sheet approximation and solved the horizontal force balance equations using a finite difference approach. However, none of the proposed models were satisfactory at matching both the stress indicators and strain rate observations, which raised questions about the validity of the isostatic assumptions and about the use of the geoid as a proxy for GPE.

Based on stress indicators, gravity, Global Navigation Satellite System (GNSS) data, and analysis of topography data, Cloetingh et al. (2002) suggested that the consistently oriented large-scale intraplate deformation in Iberia resulted from lithospheric folding. In their model, large-scale folding results from the partial decoupling between crustal and mantle layers in response to shortening, which they propose results from forces acting both at the north (during the Eocene-early Miocene) and south (from Miocene to present-day) boundaries of Iberia. Folding causes lateral density variations at the lithospheric scale due to topography and crustal thickening, therefore causing GPE gradients.

In this study, we present a new estimation of GPE in Iberia and investigate its contribution both to the net stress field and to the deformation patterns currently observed. Following previous studies that address the contribution of body forces in the context of plate dynamics (i.e., Becker & O'Connell, 2001; Bird et al., 2008; Flesch et al., 2007; Ghosh, Becker, et al., 2013; Lithgow-Bertelloni & Richards, 1998), we compare numerical model predictions to observed stress and strain rate patterns. New stress indicators and strain rate models reveal with unprecedented detail distinct deformation patterns in Iberia. We characterize the present-day stress field of Iberia using stress indicators from the latest release of the World Stress Map, WSM2016 (Heidbach et al., 2016), complemented by recent analysis of high-quality instrumental earthquakes in Iberia that identified regions where different faulting styles prevail (Custódio et al., 2016). In addition, we present a new computation of the strain rate field, based on dense and accurate geodetic velocity estimations (Neres et al., 2016; Palano et al., 2015).

In order to assess the contribution of GPE-induced stress as a driver of deformation, we build upon the latest finite element neotectonic model of Iberia by Neres et al. (2016). Because it is based on a robust lithospheric structure, both at crustal and subcrustal levels, the Neres et al. (2016) neotectonic model includes an improved estimate of GPE and respective induced stress. However, in previous modeling the GPE stress was only integrated as part of the net field, and its individual contribution was not assessed. The main goal of this study is to isolate the GPE contribution from the other driving forces and to evaluate its relative impact on intraplate deformation in Iberia. To this end, we compare the GPE contribution with the total Neres et al. (2016) model, which focuses on the geodynamics of the Nubia-Eurasia (NU-EU) plate boundary region, while also ensuring the best fit to data in the intraplate domain, thus reproducing reliably the current stress and strain rate fields for intraplate Iberia and surrounding regions. We take advantage of a self-consistent modeling strategy based on the finite element method, which allows for a better quantification of the acting forces, as well as for a better definition of the state of stress and lithospheric deformation patterns.

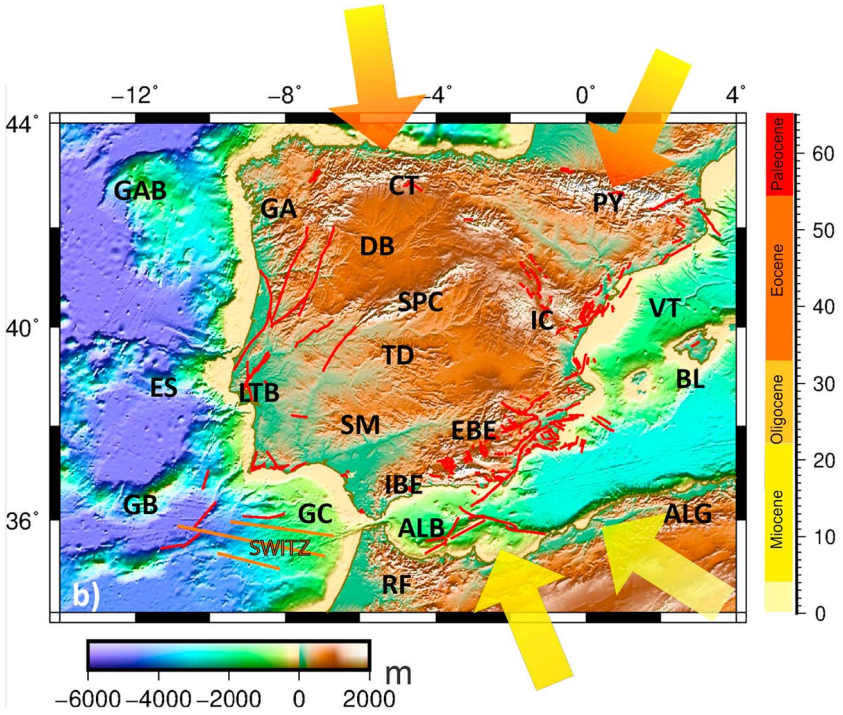

Figure 1. Topo30 digital elevation model of Iberia (ftp://topex.ucsd.edu) and fault traces from the Quaternary Active Faults of Iberia database (García-Mayordomo, 2012). Colored arrows indicate shortening directions during the Eocene-lower Miocene and Miocene to present-day periods (colors correspond to different time periods, as identified in the color scale). Main topographic features: CT: Cantabria Mountains, PY: Pyrenees, GA: Galicia Massif, DB: Douro Basin, SPC: Spanish Central System, LTB: Lower Tagus Basin, IC: Iberian Chain, TD: Toledo Mountains; SM: Sierra Morena; VT: Valencia Trough, BL: Baleares Islands, EBE: External Betics, IBE: Internal Betics, ALB: Alboran Sea, RF: Rif Mountains; GAB: Galicia Bank, ES: Estremadura Spur, GB: Gorringe Bank, GC: Gulf of Cadiz; SWITZ: Southwest Iberia transform zone.

2. Geodynamic Framework

The Iberian Peninsula (Figure 1) is the southwesternmost region of the Eurasia continental lithosphere. It lies to the north of the Nubia-Eurasia plate boundary, along the transition between the western Mediterranean and the Atlantic Ocean domains. Iberia covers a transition from an intraplate setting in the north to a diffuse plate boundary zone at its southern limit. Although the rates of seismicity are higher along the plate boundary zone, intraplate seismicity is also significant, with moderate to high-magnitude earthquakes documented in both the historical and paleoseismological records (e.g., Cabral, 2012; Custódio et al., 2016; García-Mayordomo, 2012; Martín-González et al., 2012; Rockwell et al., 2009). The geomorphology of the intraplate region exposes several stages of the tectonic evolution of Iberia. Mountain ranges with different tectonic trends record various compressive phases, particularly during the Cenozoic (Figure 1). Uplifted Variscan basement gives rise to elongated mountain ranges, which trend approximately E-W and NE-SW (e.g., Cantabria Mountains, Spanish Central System, Toledo Mountains, Sierra Morena, and External Betics). The origin of these trends has been associated with the N-S to NW-SE convergence between the Nubia-Iberia-Eurasia plates (Alpine orogeny), first along the northern Iberian border during Eocene-lower Miocene times (the Pyrenean orogeny) and subsequently along the southern Iberia border (the Betic orogeny; Casas-Sainz & De Vicente, 2009, and references therein; Cloetingh et al., 2009). In the first stage, the N-S collision between Iberia and Eurasia caused subduction of Iberian lithosphere under the Eurasian plate, with the consequent inversion of Mesozoic rift basins and uplift of the Cantabria-Pyrenean ranges along the northeastern border of Iberia. Tectonic deformation propagated into the interior of the Iberian Peninsula, where it was accommodated by crustal buckling and reactivation of left-lateral NNE-SSW strike-slip fault corridors. The main crustal-scale folds and their related thrusts are found in the Spanish Central System (SCS), the Toledo Mountains (TM), and the Sierra Morena (SM, Figure 1). The accommodation of the N-S convergence was completed by a process of tectonic inversion of the eastern Mesozoic rift basin in the easternmost part of Iberia, resulting in the formation of

the Iberian Chain (IC). In some sectors of the Iberian Chain, oblique inversion took place, with the main previous structures (NW-SE normal faults) acting as right-lateral strike-slip faults (De Vicente & Vegas, 2009).

When the main Pyrenean orogenic process ceased, in mid-Oligocene to early Miocene times, the Nubia-Eurasia NNW-SSE convergence became mostly accommodated along the southern margin of Iberia, with northward dipping subduction of the African oceanic plate in the Mediterranean realm. During this process, back-arc basins were formed, which were later accreted to the northern margin of Africa, while the terranes forming the Internal Betics drifted westward. The Gibraltar Arc results from the westward expulsion of these continental blocks, associated to the rollback of the subducted oceanic slab during the closure of the Mediterranean Sea (Gutscher et al., 2012; Lonergan & White, 1997; Royden, 1993; Spakman & Wortel, 2004). It is currently debated whether subduction underneath Gibraltar is still active and whether it can promote lithospheric weakening, thus favoring the propagation of subduction into the Atlantic (Duarte et al., 2013). In Pliocene to present times, after continental collision, the stress field rotated from NNW-SSE to WNW-SSE (Ribeiro et al., 1996; Rosenbaum et al., 2002) and a 600-km-long dextral strike-slip shear zone formed west of the Gibraltar Arc—the SWIM strike-slip transform zone—accommodating part of the motion between the Eurasian and Nubian plates (Zitellini et al., 2009).

Since the late Miocene, Nubia-Eurasia convergence has been accommodated along the present-day plate boundary south of Iberia. Regional thin-shell neotectonic models confirm a plate tectonic framework with convergence of the Nubia plate toward Eurasia plate, occurring at a rate of 4.5–6 mm/yr, and oriented NW-SE to WNW-ESE, as estimated from both GNSS and geological constraints (Cunha et al., 2012; Fernandes et al., 2003; Neres et al., 2016). These velocity and kinematic data are in good agreement with SH_{max} stress indicators from earthquake focal mechanisms and geologic indicators (e.g., Palano et al., 2013; Ribeiro et al., 1996; Silva et al., 2017; Stich et al., 2010). Onshore fault kinematic indicators (Cabral, 1989; Ribeiro et al., 1996) show a predominant NW-SE to WNW-ESE oriented SH_{max} in Quaternary times. Offshore SW Iberia, various authors (e.g., Terrinha et al., 2003, 2009; Zitellini et al., 2009) have shown that Pliocene-Quaternary reactivation of faults in SW Iberia is compatible with WNW-ESE oriented SH_{max}. The resulting deformation is mostly accommodated by thrusting and wrenching along a 600-km-long and 100-km-wide belt of deformation, which outlines a diffuse plate boundary (Koulali et al., 2011; Zitellini et al., 2009). The southwestern sector offshore Iberia (Gulf of Cadiz) is characterized by a wide (~200-km) belt of seismic activity (Buforn et al., 1995; Stich et al., 2010; Zitellini et al., 2009). In this region, the most active structures are NE-SW thrust faults and WNW-ESE right-lateral strike-slip faults (Duarte et al., 2011; Terrinha et al., 2009). Immediately to the east, in the Alboran domain, earthquakes and tomographic images reveal a lithospheric slab extending to depths of ~600 km (Mancilla et al., 2015; Villaseñor et al., 2015). Recent models indicate that surface deformation in this sector is driven by WSW directed mantle basal shear traction (Neres et al., 2016). This suggests that subduction-related processes beneath the Gibraltar Arc may still be active at present, although at low rate (Duarte et al., 2013; Gutscher et al., 2012). Farther to the east, interpretations of geodetic velocities suggest that the western Mediterranean Basin may be fragmented into independent tectonic blocks, which may be responsible for transferring part of the Eurasia-Nubia convergence rate into the Iberian domain (Palano et al., 2015). GNSS data also strongly suggest clockwise rotation of Iberia with respect to stable Eurasia, possibly driven by the right-lateral oblique collision between Africa and Iberia (Palano et al., 2015).

3. GPE in Iberia

Lithostatic pressure forces are gravitational body forces that arise from density-anomaly moments. The capacity of these anomalies to give rise to lithospheric deformation is determined by the product of the depth (z) and magnitude of the density anomalies ($\Delta\rho$) (Artyushkov, 1973; Fleitout & Froidevaux, 1982). The GPE per unit area is defined as the integrated difference in vertical stress (σ_{zz}) between two lithospheric columns: one at an arbitrary point and the other at a standard mid-ocean ridge (R; e.g., Pascal, 2006), from the top of topography (or sea level in oceanic domains; e) down to a reference level (H):

$$\mathrm{GPE} = \int_e^H \left(\sigma_{zz}(z) - \sigma_{zz}^R(z)\right) dz = \int_e^H \left[\int_e^z g\Delta\rho dh\right] dz \quad (1)$$

Here we assume that H is the varying base of the lithosphere (as defined in section 4). The density is estimated at depth with 1-km steps for the crust and for the upper mantle as $\rho = \rho_0 (1 - \alpha_T T)$, where ρ_0 is the

density at the ground surface (2,889 kg/m for the crust and 3,332 kg/m for the mantle), α_T is the volumetric thermal expansion (2.4×10^{-5} and 3.94×10^{-5} K^{-1}, respectively), and T is the temperature determined as in Bird et al. (2008) and Carafa, Barba, et al. (2015).

Lateral variations of GPE give rise to gravitational potential stresses, which are defined as the horizontal gradients of GPE averaged over the thickness of the lithosphere.

Figure 2 shows the GPE in Iberia computed according to equation (1). A Pearson's correlation coefficient of 0.87 indicates a clear correlation between regions of high GPE and regions of elevated topography (Figure 1). The correlation between GPE and topography is also evident when the comparison is made along two representative profiles (Figure 3; other profiles have been tested, showing similar results). The profiles are tracked for small circles centered on the Nubia-Eurasia Euler rotation pole at 30 (Eocene-lower Miocene) and 5 Ma (Miocene to present; Rosenbaum et al., 2002). For each track, the periodic components of both GPE and topography were evaluated using Singular Spectral Analysis (SSA), a form of principal component analysis. We used a standard algorithm to decomposed the detrended and normalized profiles into principal components (the eigenvalues) and empirical orthogonal functions (EOFs; Vautard et al., 1992). We applied a chi-square significance test (150-km window length) in order to identify the most significant reconstructed components. We then evaluated their contribution to the total variance of the spatial data. A window length of 150 km is one tenth of the total number of points in the series, which is consistent with the recommendations of Vautard et al. (1992).

Table 1 lists the wavelengths of the leading modes of variability, which correspond to the first three empirical orthogonal functions. The lowest-frequency component (wavelength ~1500 km) corresponds to the diameter of the continental area. RC-1 is not shown alone but is included in the composite of the reconstructed components (cRCs, the superposition of the first three principal components). The two other components (RC-2 and RC-3) are interpreted as representing the dominant modes of large-scale lithospheric folding. The topography and GPE have matching folding wavelengths (371 and 135 km, with less than 2% of difference in variance) along the Eocene-lower Miocene track. However, there is no match between folding wavelengths along the Miocene-present-day track (Table 1). These results are in agreement with the geologic history of the Iberian Peninsula, given that the elongated ranges that dominate the plate interior are mainly associated to the N-S to NW-SE convergence between the Nubia-Iberia-Eurasia plates that took place during Eocene-lower Miocene times (the Pyrenean orogeny; e.g., Casas-Sainz & De Vicente, 2009).

4. Modeling Stress and Strain Rate: TOTAL and GPE Models

We present the stress and strain rate responses of two finite element models for Iberia: one that includes only the stresses due to lithospheric pressure forces (hereafter *model GPE*) and another one that represents the net driving forces (hereafter *model TOTAL*).

Stress and strain rate computations for the Iberia Peninsula and surrounding regions are performed using the code SHELLS (version 3: Bird et al., 2008, and references therein, in particular Kong and Bird, 1995). SHELLS is a thin-shell finite element code that solves the stress equilibrium equation and computes the surface velocity field, continuum strain rates, horizontal stress field, and fault slip rates. Although the differential equations are solved on a 2-D grid, it integrates the 3-D structure of a two-layered lithosphere (crust and lithospheric mantle), resulting in a so-called 2.5-D code. For this work, we adopt the lithospheric model of Neres et al. (2016), which is defined for a finite element grid with average 27-km side length elements. The ground surface of the lithosphere is based on the ETOPO1 (Amante & Eakins, 2009), and the Moho surface is taken from the EPcrust model (Molinari & Morelli, 2011; Figure 4). The temperature in depth is determined using OrbData5 (Bird et al., 2008) and data records from the International Heat Flow Commission database (http://www.heatflow.und.edu/data.html), whereas the base of the lithosphere is determined by using the *S* wave tomography model S40RTS (Ritsema et al., 2011) following the scheme of Carafa, Barba, et al. (2015). For further details on the input lithospheric data and modeling method to determine the lithospheric structure see Neres et al. (2016) and Carafa, Barba, et al. (2015).

For each layer, the brittle-ductile rheology (relation between vertically integrated stress and the horizontal strain rate tensors) is given by frictional sliding and power law dislocation creep, respectively (see Bird and Piper, 1980, Bird, 1989, 1999, and Carafa and Barba, 2011, for details on the rheology used in SHELLS).

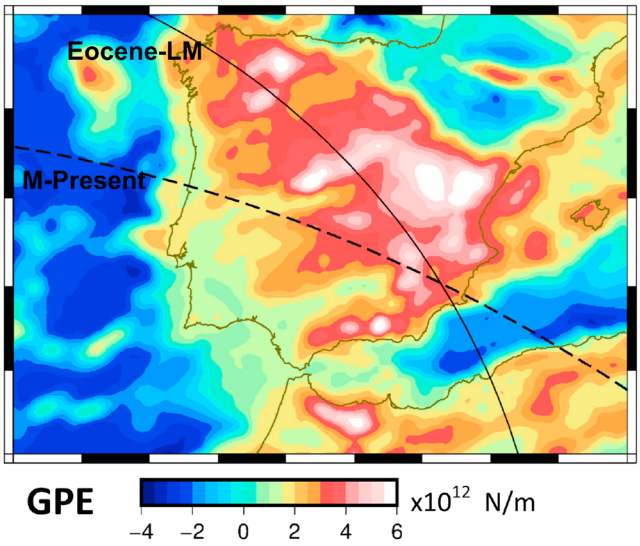

Figure 2. GPE (gravitational potential energy) calculated from the lithospheric model of Neres et al. (2016). Small circles about the Nubia-Eurasia Euler poles (solid line for the Eocene-lower Miocene and dashed line for the Miocene to present) as estimated by Rosenbaum et al. (2002).

SHELLS may include four types of driving forces: (1) lithostatic pressure forces, (2) tectonic forces related to velocity boundary conditions at plate edges, (3) basal shear tractions applied at the base of plates, and (4) forces on faults. In the version used here, SHELLS implements a *hybrid* approach, in which kinematic constraints are iteratively converted into diffuse basal shear stresses that drive plate interiors toward the best dynamic reproduction of real Earth observations. The modeling approach of SHELLS is detailed by Bird et al. (2008).

Neres et al. (2016) used SHELLS to carry out neotectonic modeling for the region encompassing Iberia, North Africa, and NE Atlantic. They searched, among 5,240 simulations, for the most reliable modeling parameters, boundary conditions, and geodynamic scenarios. Their preferred model, which best fits observed GNSS velocities, SH_{max} directions, and seismic strain rates calculated from instrumental earthquakes, has edge velocity boundary conditions defined by the new geodetic SEGAL2013 angular velocity model (which was tested

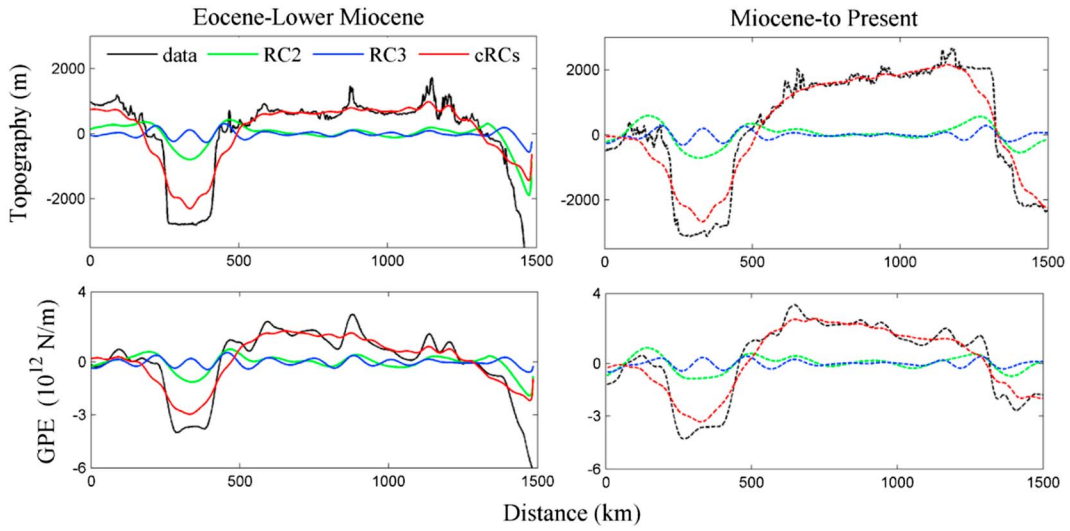

Figure 3. Analysis of periodic components along profiles of topography and GPE tracked along the small circles in Figure 2. (black solid/dashed lines). Partial reconstructions of the data based on the leading components of folding EOF 2 (green solid/dashed lines) and EOF 3 (blue solid/dashed lines). The red solid/dashed lines are the composite of the principal components (cRCs = RC1 + RC2 + RC3) listed in Table 1. See more detailed explanations in the text.

Table 1
Oscillatory Modes Derived From SSA Applied to Topography and GPE

	Topography		GPE		
EOF	Wavelength (km)	Variability (%)	Wavelength (km)	Variability (%)	
1	1,485	74	1,486	76	Eocene - Lower Miocene
2	371	20	372	18	
3	135	3	135	4	
1	1,689	86	1,691	84	Miocene - Present
2	563	10	338	13	
3	140	1	169	2	

Note. Identification of the first three empirical orthogonal functions (EOFs) and their relative contribution to the total variance of the spatial data.

against the geological-scale MORVEL pole by DeMets et al. (2010)) and includes an independent Alboran plate driven by a WSW directed basal traction related to forces induced by the Rif-Gibraltar slab. We highlight its accuracy in describing the observed stress field, with SH_{max} misfit scoring lower than 15°.

In the present work, we take the preferred model of Neres et al. (2016) as our TOTAL model. Therefore, TOTAL includes the four classes of driving forces listed above: lithostatic pressure forces (due to gravitational potential energy, GPE); intralithospheric collisional side forces, initially imposed by velocity boundary conditions and iteratively regulated; basal shear tractions that are mainly important in driving the Alboran domain; and forces on fault surfaces.

The GPE model was built for the present study, and further details on physical parameters are given in section 3. In order to isolate the GPE contribution, we modified the SHELLS code by *turning off* the three other driving mechanisms: we set all velocity boundary conditions to zero, disabled basal shear tractions, and locked all fault elements. Thus, the GPE model describes the response of the lithosphere to the stresses imposed by GPE only.

The SH_{max} direction and amplitude (defined as the vertically integrated most compressive stress divided by the lithospheric thickness) for the GPE and TOTAL models are shown in Figures 5a and 5b. The respective modeled strain rates are represented in Figures 6a and 6b. Sections 6 and 6.2 discuss in detail the GPE and TOTAL models.

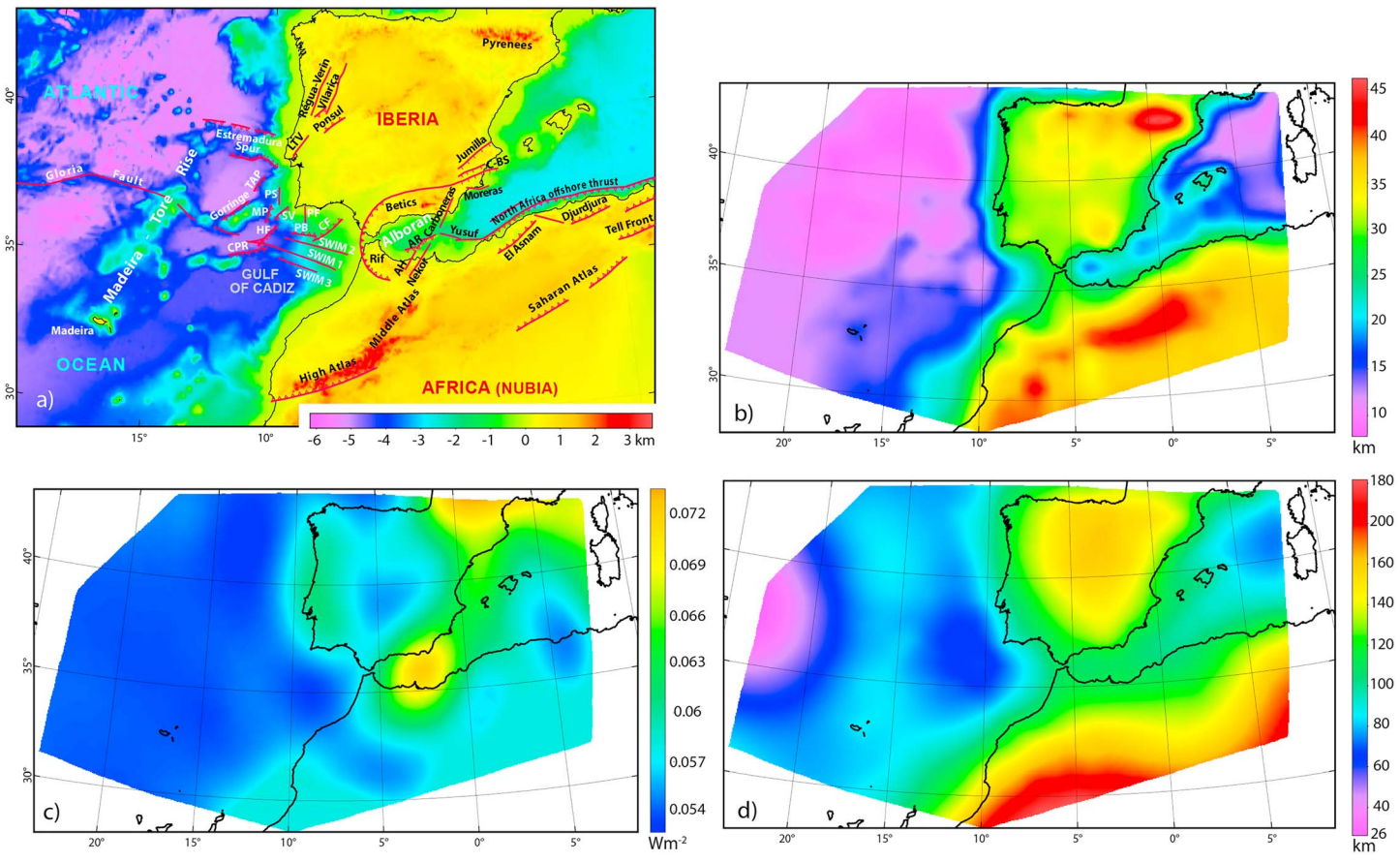

Figure 4. Lithospheric data input to the finite element modeling. (a) Elevation and faults (faults are only input for the TOTAL model). (b) Thickness of the crust. (c) Heat flow and (d) total lithospheric thickness. See section 4 and Neres et al. (2016) for details.

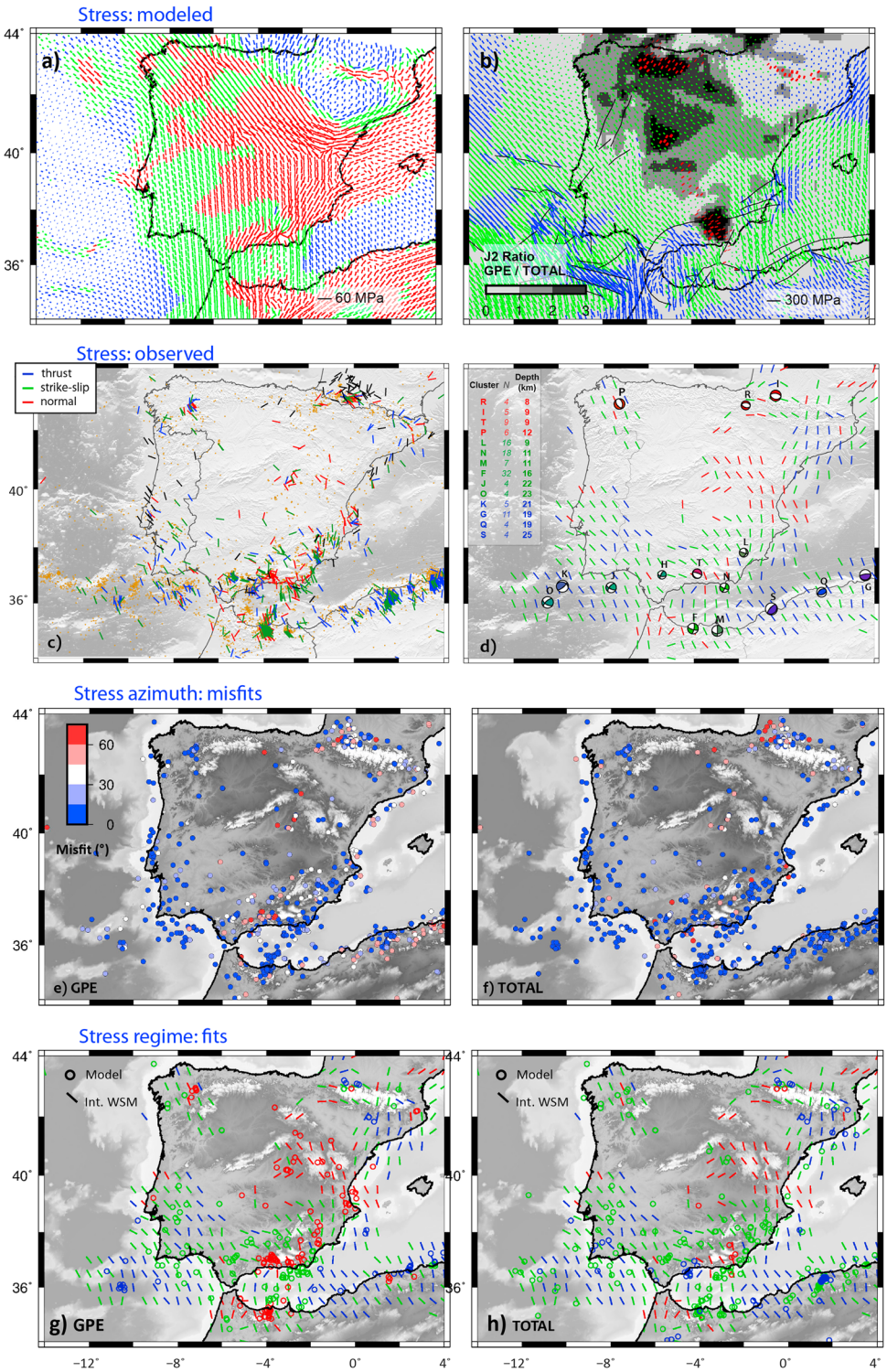

Figure 5. (a, b) Direction of SH_{max} and stress regime (red: normal; green: strike slip; blue: thrust) for GPE model (a) and TOTAL model (b): Note the difference in scales. (b) Also shows the spatial variation of the ratio between J2-GPE and J2-TOTAL. The ratio is saturated at J2-GPE/J2-TOTAL = 3. (c) Horizontal stress indicators: SH_{max} direction and stress regime from the WSM2016 database (Heidbach et al., 2016). Small yellow dots mark the epicenters of earthquakes that occurred between 2000 and 2014, which were used by Custódio et al. (2016) for the epicenter clustering analysis. (d) Interpolated WSM data: SH_{max} and stress regimes. Overlaid are representative mid-focal mechanisms of hypocenter clusters and respective faulting regime, as calculated by Custódio et al. (2016); mean depths of earthquake clusters are listed in the inset. (e, f) SH_{max} misfits for (e) GPE model and (f) TOTAL model: angular difference in SH_{max} azimuth between each model and interpolated WSM indicators, minus the uncertainty of WSM indicators. (g, h) Stress regime fits for GPE model (g) and TOTAL model (h): circles indicate fit between modeled stress regime and faulting regime of the WSM indicators.

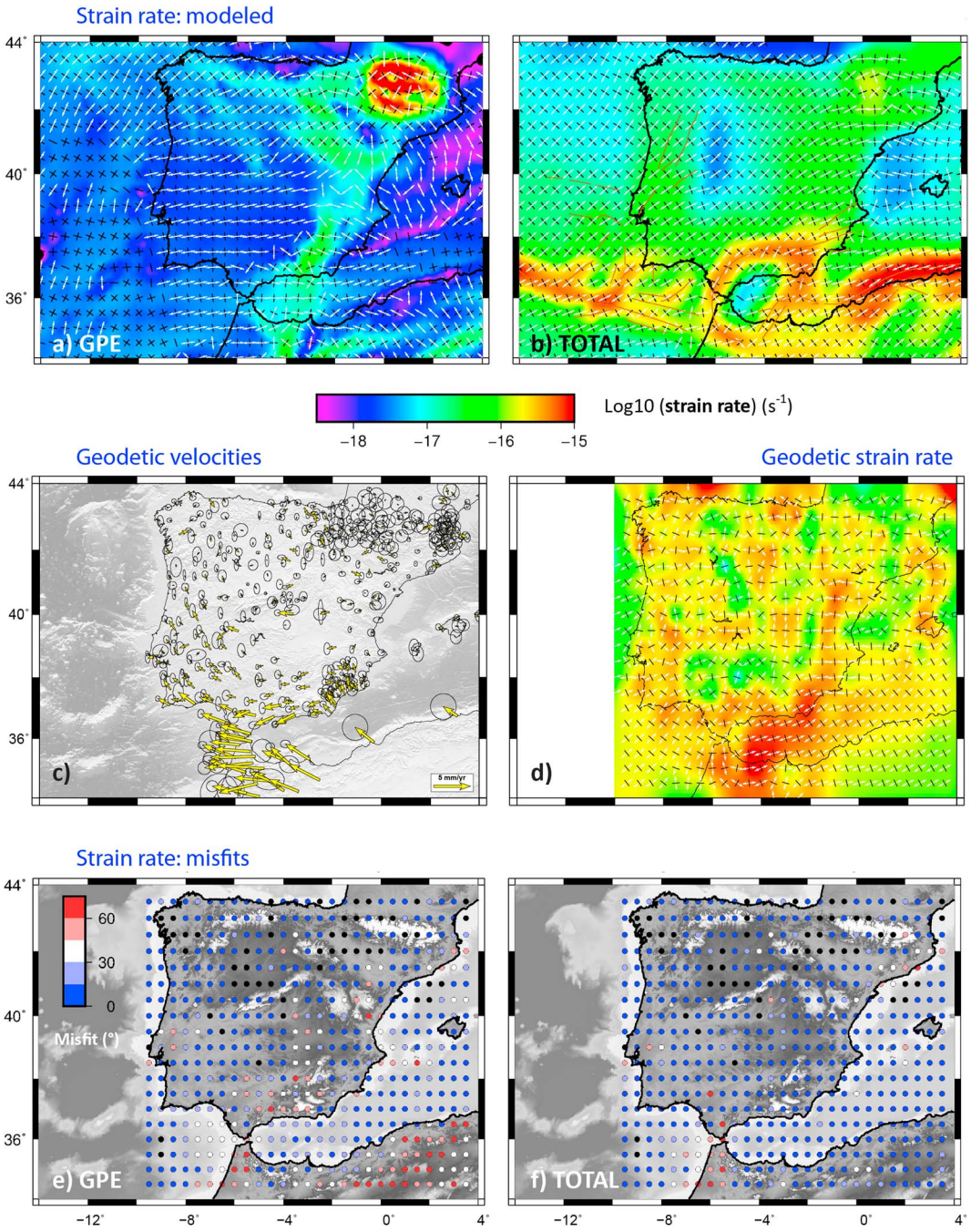

Figure 6. (a, b) Modeled strain rate field for GPE model (a) and TOTAL model (b). Greatest extensional ($\dot{\varepsilon}_{H_{max}}$ in white) and contractional ($\dot{\varepsilon}_{h_{min}}$ in black) horizontal strain rate directions are superimposed on strain rate magnitude. Note that $\dot{\varepsilon}_{h_{min}}$ has the same direction as SH_{max} in Figures 5a and 5b. (c, d) Geodetic velocity and strain rate fields for Iberia as computed in this study. (c)GPS velocities and 95% confidence ellipses in a fixed Eurasian reference frame. (d) Geodetic strain rates calculated from the velocity field. Arrows represent the greatest extensional (white) and contractional (black) horizontal strain rates. Color in background represents the strain rate magnitude. (e, f) Strain rate misfits for GPE model (e) and TOTAL model (f): difference in $\dot{\varepsilon}_{h_{min}}$ azimuth between each model and data, minus the uncertainty of each data point. Misfits larger than 75° are colored in black.

5. Observed Stress and Strain Rate Patterns in Iberia

In this section we describe observations of the current state of stress and surface deformation in Iberia. These data will be compared in the next section to the GPE and TOTAL models.

5.1. Stress Indicators

A recent image of the crustal regional stress field in Iberia is provided by the World Stress Map (WSM2016; Heidbach et al., 2016; Figure 5c) database, which contains stress indicators (e.g., orientations of the maximum horizontal compressional stress SH_{max} and associated stress regimes), namely, from focal mechanisms and also from borehole breakouts, drill-induced fractures, borehole slotters, overcoring, hydraulic fractures, and geological constraints. For this work, we considered only high-quality stress indicators A, B, and C, which estimate SH_{max} with maximum errors of ±15°, ±20°, and ±25°, respectively, leaving out poorer indicators of qualities D and E. To ease the interpretation of WSM2016 indicators in terms of regional stress patterns, we interpolated the WSM2016 data set using the SHINE interpolation algorithm for clustered data (see Carafa and Barba, 2013, and Carafa, Tarabusi, et al., 2015, for additional details; Figure 5d).

SH_{max} orientations in west and southwest Iberia and along the north coast of Algeria are consistently NW-SE, suggesting that the present-day stress field in these regions is generally controlled by the ongoing oblique convergence between Nubia and Eurasia (Custódio et al., 2016; De Vicente & Vegas, 2009; Neres et al., 2016; Palano et al., 2013,2015; Ribeiro et al., 1996; Stich et al., 2006). The patterns of SH_{max} in the Alboran Sea, Betic-Rif arc, and central and northeast Iberia, encompassing the Pyrenees, deviate from the NW-SE direction of plate convergence, suggesting the existence of other mechanisms at work.

At first glance, WSM2016 indicators might suggest the coexistence of all three stress regimes in some regions, namely, in the Pyrenees and in the Betics-Rif system (Figure 5c). However, a detailed inspection reveals that normal faulting stress indicators localize in regions of topographic highs, while strike-slip and thrust faulting regimes are ubiquitous. This becomes more evident when we analyze the interpolated data (Figure 5d). Normal stress regimes appear to have a regional importance mainly in the Iberian Chain and also in the eastern Betics, Rif, and Pyrenees. Elsewhere, the regional stress is dominated by strike-slip and thrust faulting regimes.

5.2. Hypocenter Clusters and Mid-Focal Mechanisms

Figure 5d also shows the focal mechanisms representative of the style of faulting of individual earthquake clusters, as computed by Custódio et al. (2016): Clusters were first defined as groups of at least 20 earthquakes located within 20 km of each other. Mid-focal mechanisms (mid-FMs) were then computed for clusters with at least four focal mechanisms available. The mid-FM is the focal mechanism that minimizes the angular distance to all other focal mechanisms in the cluster. The angular distance between two focal mechanisms is defined as the minimum rotation angle between their *P*, *T*, and *B* axes or equivalently as the minimum rotation angle between the possible slip vectors of two focal mechanisms (Kagan, 1991).

Based on the analysis of focal mechanisms, Custódio et al. (2016) identified three dominant faulting styles (Figure 5d):

1. The most frequent focal mechanisms are strike-slip earthquakes, which are usually right lateral on NW-SE oriented faults or left lateral on NE-SW oriented faults. They prevail in offshore western Iberia (Clusters O and J) and in the Trans-Alboran shear zone (Clusters F, L, M, and N). The Trans-Alboran shear zone and its onshore northeastward prolongation in SW Iberia, along active faults such as the Carboneras Fault, is a wide region of left-lateral strike-slip faulting that cuts across the Alboran Sea (e.g., Bousquet, 1979; De Larouzière et al., 1988; Leblanc & Olivier, 1984; Mancilla et al., 2013). Earthquakes offshore western Iberia have a reverse component and moderate mean hypocentral depths (>20 km), whereas those in the Trans-Alboran shear zone are shallower (<20 km) and exhibit a normal component.
2. The second most common type of focal mechanisms indicates reverse faulting with NW-SE oriented subhorizontal *P* axis. They are found dominantly along the northern coast of Algeria. Two clusters can be distinguished in this region (Clusters S and Q), both of which display reverse focal mechanisms with ENE-WSW oriented fault planes, parallel to the orientation of the main faults and topography of the region. In the plate boundary region south of Portugal, Cluster K also has a mid-FM indicating reverse motion with a small strike-slip component. Similar to northern Algeria, the region offshore SW Portugal is marked by major thrust faults and topographic highs striking NE-SW. In both regions, reverse mid-FM have mean depths around 20 km.
3. The third type of focal mechanisms corresponds to oblique normal fault earthquakes with SW-NE oriented *T* axis. These earthquakes occur in southern Spain and in northern Iberia. Cluster T, in southern Spain, is

associated with extension in the Granada basin (Stich et al., 2010). In NW Spain, Cluster P strikes NNW-SSE, parallel to the strike of the Vilach-Baralla and Becerre faults (Basili et al., 2013; García-Mayordomo, 2012). In the Pyrenees, Clusters R and I strike WNW-ESE, which for Cluster I coincides with the direction of elongation of the clustered earthquakes. All normal mid-FMs have shallow mean depths, ranging between 8 and 12 km.

5.3. Geodetic Velocity Field

We computed a new velocity field by integrating new and published GNSS data that covers the investigated area. This new velocity field updates those of Neves et al. (2014) and Neres et al. (2016), using larger time spans for most of the stations and including additional new continuous stations operated by regional and national networks established for mapping, engineering, and land planning purposes (see also Neres et al., 2016). In particular, we analyzed GNSS observations acquired from 192 permanent stations (see http://ntrip.rep-gnss.es/ for the location of the majority of the stations) with a minimum time span of 3.5 years (and a maximum of 21 years), until the end of 2016. The methodology used to compute the velocity fields was the same as in previous studies (Neres et al., 2016; Neves et al., 2014). First, we estimated daily time series using the GIPSY-OASIS v6.3 software package (Lichten et al., 2006), which uses undifferentiated data to process each station individually using the strategy of Precise Point Positioning (Zumberge et al., 1997). The entire data set was reprocessed using consistent state-of-the-art models and parameters, namely, an elevation cutoff of 7.5°, the VMF1GRID mapping function (Boehm et al., 2009), NASA's Jet Propulsion Laboratory (JPL) precise orbit and clocks (available at http://sideshow.jpl.nasa.gov), GOT4.8 ocean loading corrections (available at http://holt.oso.chalmers.se/loading/), and antenna phase center corrections provided by IGS-IGS08 model (Schmid et al., 2016). The estimated daily solutions were then aligned with ITRF2008 by performing a Helmert (seven-parameter) transformation based on a network of about 30 IGS stations (depending on data availability) globally distributed. Finally, we computed the velocity field using the Hector software package (Bos et al., 2013), which estimates the secular motion of each station independently for each component and uses a combination of power law (spectral density different of zero) and white noise (spectral density equal to zero) models to account for existing noise in the time series. This allows us to obtain a more realistic estimation of the velocity uncertainties (by a factor of 5 to 10 greater than the formal errors of a least squares fit). Hector also estimates the magnitude of detected offsets and seasonal (e.g., yearly and half-yearly) signals. From the total 192 processed stations, 21 were excluded from further analysis due to various issues, including reported unstable monuments, no linear secular motion (including in the vertical component), too many data gaps, and/or short time series.

This new set of solutions was rigorously integrated with further solutions reported by Palano et al. (2015), which provides a higher data density in southeast Iberia and northern Morocco, and by Rigo et al. (2015), which includes a more extensive coverage of the Pyrenean mountain range. The final geodetic velocity field presented is thus as complete as possible over the investigated area (see Table S1 in the supporting information for details). The three sets of solutions were merged using VELROT, a subroutine of the GAMIT/GLOBK software (http://www-gpsg.mit.edu/). Palano et al. (2015) and Rigo et al. (2015) solutions were aligned to the ITRF2008 reference frame defined by our solution with a six-parameter transformation (the components of the rate of change of translation and rotation) obtained by minimizing the horizontal velocity residuals between common sites. In such a computation, we used 18 and 6 common sites for Palano et al. (2015) and Rigo et al. (2015) solutions, respectively. The root-mean-square of the horizontal components for all the common stations used in the computation is less than 0.33 mm/yr, showing a good agreement between the different solutions. Finally, we rotated our ITRF2008 velocity field to a fixed Eurasian reference frame (latitude 55.050°N, longitude −99.455°E, rotation rate 0.258; see Cannavò and Palano, 2016, for details) in order to better identify the pattern of crustal deformation in the Iberia region. The resulting velocity field is represented in Figure 6c and listed in Table S1. Some previously established first-order active kinematic features of the study area are evident: (1) clockwise rotation of Iberia with respect to Eurasia, (2) fragmentation of western Mediterranean Basin into different crustal blocks, and (3) slow (<1-mm/yr) crustal deformation across the Pyrenean mountains.

5.4. Geodetic Strain Rate Field

We computed a continuous 2-D strain rate tensor field (and associated uncertainties) over the study area using our new velocity field. As described in the supporting information Text S1, we first estimated the

continuous velocity field and associated uncertainties on a regular 0.5° × 0.5° grid using a *spline in tension* technique (Smith & Wessel, 1990; Wessel & Bercovici, 1998). We excluded all sites with suspicious movements (usually larger than 150%) with respect to nearby sites from the computation (see Table S1). In a final step, the strain rate tensor was estimated as the derivative (computed via finite differences) of the interpolated velocities at the nodes of each grid cell (e.g., Hackl et al., 2009, and references therein). Uncertainties related to the principal strain rates ($\dot{\varepsilon}_{H_{max}}$, $\dot{\varepsilon}_{h_{min}}$) and the principal angles (φ_{max} and φ_{min}, direction of $\dot{\varepsilon}_{H_{max}}$ and $\dot{\varepsilon}_{h_{min}}$, respectively) were also computed according to Farolfi and Del Ventisette (2017; Text S1).

The estimated strain rates, spanning the 10^{-17}–10^{-15} s^{-1} values interval, are shown in Figure 6d: the arrows show the greatest extensional ($\dot{\varepsilon}_{H_{max}}$) and contractional ($\dot{\varepsilon}_{h_{min}}$) horizontal strain rates, whereas the color scale in the background shows the strain rate magnitude. The uncertainties $d\varphi$ related to the direction of $\dot{\varepsilon}_{h_{min}}$ are reported in Figure S1.

The highest strain rates are observed along the diffuse plate boundary zone between Eurasia and Nubia. In this region, the strain rate field shows generally NNW-SSE oriented shortening of values up to 1×10^{-15} s^{-1}. In the Alboran domain, the shortening strain rate axes are coupled with WSW-ENE extensional strain rate axes of the same order of magnitude (~$0.8–1.2 \times 10^{-15}$ s^{-1}). East of Gibraltar to the Baleares islands the NNW-SSE shortening is approximately constant. The extensional component diminishes abruptly across Gibraltar to the west and gradually to the east. All of these areas are characterized by uncertainties in the direction of $\dot{\varepsilon}_{H_{max}}$, generally lower than 30°. Some sectors of the central and northern Iberian Peninsula are characterized by small to moderate (up to 0.9×10^{-15} s^{-1}) extension-contraction patchy strain rate patterns. This feature may result from random velocity components observed between close stations, which may reflect local processes such as geodetic monument instability, water table level changes, ground humidity content, or bedrock thermal expansion (Palano et al., 2015). Therefore, the observed extension-contraction patchy pattern might not be geodynamically significant. These sectors are also characterized by uncertainties in the direction of $\dot{\varepsilon}_{H_{max}}$ generally larger than 30° (and somewhat larger than 90° as observed in some areas of NW, central, and NE Iberia), reflecting both the above mentioned random velocity components and the low deformation rate observed (only a few of the velocities are significantly different from zero within 95% confidence; Figure 6d). Nevertheless, we note that some clusters of extension in the northern central part of Iberia coincide with elevated regions (Duero Basin, Toledo Mountains, and Iberian Chain). For regions with lower density of GNSS stations (e.g., Castilla-La-Mancha and northern Algeria), the regional strain rate field estimation is less well constrained; therefore, the information concerning these regions should be considered with caution.

6. Analysis of GPE and TOTAL Stress and Strain Rate Fields

6.1. GPE and TOTAL Stress Fields

6.1.1. GPE Stress Field

The orientation and magnitude of SH_{max} and fault stress regimes due to the modeled gravitational potential stresses (model GPE) are shown in Figure 5a. SH_{max} is consistently NW-SE oriented along the whole Atlantic domain and in most of north and central Iberia. On top of the Iberian Chain and Pyrenees, it deflects to WNW-ESE, becoming nearly parallel to the strike of these ranges. From the Rif to south Portugal through the Gulf of Cadiz it is N-S oriented.

Within the continental areas, the excess in GPE (with respect to neighboring oceanic domains) results in horizontal tensile forces. These create normal faulting stress regimes in regions of GPE maxima (mountain ranges) and strike-slip faulting stress regimes in adjacent regions. Exceptions occur in the basins around the Pyrenees, where compressive regimes are induced by high GPE gradients.

Along most of the continental margins (Atlantic and North Algerian margins) the strong contrast between onshore-offshore GPE originates lateral compressive forces, which induce predominantly thrust faulting stress regimes in oceanic basins. This is, however, not the case for oceanic areas in the Valencia Trough (normal faulting) and in the Gulf of Cadiz-Alboran region (strike-slip faulting). In the Valencia Trough, extensional regimes occur because the crust is thinner than in adjacent regions. In the Gulf of Cadiz-Alboran region, strike-slip regimes are due to the low contrast between onshore and offshore elevation and crustal thickness (Figure 4). In the Atlantic domain, localized extension and abrupt changes in GPE-induced stress direction are related to the presence of seamounts, where the difference in height from regional seafloor to top of

seamount can be of ~5 km in the Gorringe Bank, ~4 km in the Estremadura Spur, and ~3.5 km in the Galicia Banks.

6.1.2. TOTAL Stress Field

Figure 5b displays the net stress field of model TOTAL, which includes the gravitational potential stresses, collisional tectonic stresses, basal shear tractions (mostly important in the Alboran domain), and forces on fault surfaces.

SH_{max} has an overall NW-SE orientation, both onshore and offshore, in agreement with the current direction of Nubia-Eurasia convergence. Clear exceptions are found in the Valencia Through and in the Alboran domain, in the latter dominated by the effect of basal shear tractions related to subduction in the Gibraltar arc. The stress orientation in the Algerian margin is clearly determined by the tectonic push of the Nubia plate.

Strike slip is the dominant faulting stress regime, both in the continent and in most of the surrounding Atlantic and Mediterranean regions. Thrust faulting stress regimes in oceanic areas are associated with offshore faults, particularly in the Gulf of Cadiz and offshore SW Iberia. A thrust regime is also dominant in the Gibraltar arc and North Africa.

In order to quantify the relative contribution of GPE to the TOTAL stress field, we computed a ratio of stress magnitudes between the two models. Both the vertical and horizontal stress components play an important role in defining the faulting style; therefore, we computed the second principal invariant of the deviatoric stress tensor (J2) as a measure of magnitude of the three principal stress components. We then computed the ratio between J2 computed at each point in the GPE model (J2-GPE) and J2 computed at each point in the TOTAL model (J2-TOT; Figure 5b). Thus, when the J2-GPE/J2-TOTAL ratio is more than 1, GPE dominates over other driving forces. Figure 5b shows that the GPE effect is concealed within the net stress field in vast regions of the model, particularly offshore, where the $|SH_{max}|$ generated by GPE (maximum values of ~60 MPa in Figure 5a) is only about 20% of the magnitude of the total $|SH_{max}|$ (maximum values ~300 MPa in Figure 5b). However, the J2-GPE/J2-TOTAL ratio is >1 in parts of the central Iberian Plateau, Cantabria, and Betics. In fact, locally, the contribution of GPE to the deviatoric stress field can be up to 3 times larger than all other contributions combined. The effect of GPE becomes evident in the form of local normal faulting regimes confined to elevated areas in Cantabria, central Pyrenees, and in a NW-SE trending corridor from the eastern Betics to the Central Massif. In most of these regions (except in central Iberia), a general good agreement between the faulting style of GPE and TOTAL is also found (Figure S2).

6.1.3. Models Versus WSM Data

The agreement between modeled stress fields with WSM2016 indicators is shown in Figure 5e for the GPE model and in Figure 5f for the TOTAL model. The angular misfit (θ) is the difference between the SH_{max} directions predicted by the model and the SH_{max} of WSM2016 indicators. The angular misfit θ is computed at every location for which there is a WSM data point (Figure 5c). We take into account the absolute uncertainty in the SH_{max} azimuth, given by the quality of the stress indicator, such that θ is the difference between model prediction and observations, minus the uncertainty. Thus, if the difference between model prediction and observations is less than the uncertainty of observations, then $\theta = 0$. The maximum difference between two SH_{max} directions is 90°. Because we subtract the uncertainty of stress indicators, which is between 15° and 25°, θ ranges from 0° to ±75°.

The angular misfit distribution shows that the stress field of model TOTAL matches the WSM SH_{max} direction better than model GPE almost everywhere (Figure 5f: 80% of the θ values have uncertainties less than 15°; Figure 5e: 50% of the θ values have uncertainties less than15°). This is especially relevant for regions along the plate boundary zone (Algerian margin, Betics, and Gulf of Cadiz), but also for the Valencia Trough and south Portugal. This observation supports that tectonic forces not only are the main driving mechanisms along the plate boundary but also influence intraplate streses. (For more details on the computational method to accurately transmit the intraplate stresses imposed by plate convergence, see Neres et al., 2016). In the Gulf of Cadiz, the high SH_{max} accuracy of the TOTAL model is furthermore significantly improved by taking into account active faults. In some regions, namely, at the north and west of Iberia and in the northern offshore, the modeled SH_{max} and respective misfits are similar for both the GPE and TOTAL models.

Figures 5g and 5h show the fit between modeled and observed faulting regimes. The main evidence is that the GPE model fits the faulting regimes of WSM2016 indicators in areas of normal faulting, where the TOTAL

model does not perform as well. This is mainly evident for the high-topography areas of the Iberian Chain, Cantabria, Rif, and eastern Betics. The local better performance of GPE may suggest that the GPE effect is underweighted in the TOTAL model, possibly due a less accurate balance of the lithostatic and collisional forces at local scales.

6.2. GPE and TOTAL Strain Rate Fields

Modeled strain rates are shown in Figure 6a for the GPE model and in Figure 6b for the TOTAL model. Because SHELLS assumes isotropy, the modeled stress and strain rate fields show similar distributions in terms of principal directions. Nevertheless, the strain rate maps emphasize several relevant aspects of the models.

The strain rate due to GPE (10^{-18}–10^{-17} s^{-1}) is on average much smaller than the strain rate of TOTAL (10^{-16}–10^{-15} s^{-1}), suggesting that body forces play a minor role in driving deformation in Iberia. However, the rates of deformation of the GPE and TOTAL models are similar over mountain ranges, such as the Iberian Chain (~5×10^{-17} s^{-1}), eastern Betics (10^{-16} s^{-1}), and Cantabria (10^{-17} s^{-1}), thus indicating that GPE is a substantial driving force in these elevated regions, in agreement with the previous stress analysis. In the Pyrenees, the high strain rates due to GPE alone (10^{-15} s^{-1}) are reduced by the effect of the forces due to Nubia-Eurasia convergence.

The highest TOTAL strain rates occur along the Nubia-Eurasia plate boundary zone and across the Gibraltar arc, in agreement with seismic activity (Figure 5c) and strain rate observations (Figure 6d). The magnitude of TOTAL strain rates is within the same range of observed strain rates; however, a number of significant differences can be recognized. For example, the high strain rates modeled for the Algerian margin do not have a geodetic correspondence. This may be a model artifact due to the lack of GNSS data in Algeria and on the Mediterranean Sea, which results in smoothing of the strain rate field across the oceanic domain up to Iberia. Such artifacts may also be present in the Gulf of Cadiz, where the oceanic faults in the model result in a strain distribution that cannot be imaged by geodesy. Conversely, moderate to high strain rates are measured both along the southeastern, southwestern, and western margins of Iberia, which are not predicted by model TOTAL.

In order to compare model-predicted strain rates with the geodetic strain rate data, we computed again an angular misfit (θ) that now gives the absolute difference in the $\varepsilon_{\mathrm{hmin}}$ directions of models and data, minus the uncertainty of the observations. Misfits are shown in Figure 6e for model GPE and in Figure 6f for model TOTAL. The angular misfit θ was computed at every location for which there was a strain rate value (0.5° × 0.5° grid), taking into account the uncertainties related to the principal angle φ (direction of $\dot{\varepsilon}_{h_{min}}$) as reported in Figure S1. Overall, the TOTAL strain rate field matches the strain data better than the GPE field, in several cases lowering the misfits from 45 to 60° to <15°. This is particularly evident for the Algerian margin, Betics, and south and SW of Iberia offshore, which is expected given their proximity to the plate boundary. However, due to the low number of geodetic observations in this area, such interpretations should be considered with caution. Large misfits remain near the Gibraltar strait, suggesting that the models still lack detail related to the Rif-Gibraltar slab dynamics. Regions where the strain rate is fit well by the GPE model alone (with misfits <30°) include the Valencia Trough region, northwest Iberia, southwest Iberia (mainland), the Spanish Central System, and the Pyrenees.

7. Discussion

Our estimation of GPE represents an improvement with respect to previous works (Andeweg, 2002; Neves et al., 2014) that results mainly from the more detailed lithospheric structure and to the variable, seismically determined lithospheric base level. In some regions, for instance, in North America, the GPE increase due to elevated topography may be reduced or even canceled by deepening of the Moho, as proposed by Jones et al. (1996). In most of Iberia, however, the excess of GPE associated with surface relief along major mountain ranges (Cantabrian Mountains, Iberian Chain, and Betics) does not seem to be completely compensated by density anomalies associated with Moho relief (Figure 4b). On the contrary, a deeper base of the lithosphere, for example, below the Iberian Chain region (Figure 4d), further contributes to increase GPE. A different situation is observed in the Pyrenees and surrounding areas, where the presence of a deep crustal root (Figure 4b) creates a negative density contrast relative to the surrounding uppermost mantle that lowers the integrated vertical stress, resulting in a regional GPE low surrounding the Pyrenees, with local maxima at the top of the highest peaks. Recent detailed tomographic models for Iberia (e.g., Chevrot et al., 2014;

Palomeras et al., 2017) show a thicker lithosphere beneath the Pyrenean region than that considered in our model. Such a deeper lithospheric base could compensate the deep Moho and increase the GPE, but we argue that this effect would not completely cancel the modeled regional GPE low. In fact, an independent estimation of GPE and associated deformation in the Pyrenees by Camelbeeck et al. (2013), which assumed as a proxy for GPE the second spatial derivative of the geoid, found similar GPE variation and deformation patterns of extension over highs and compression at adjacent regions. Genti et al. (2016) used 2-D numerical modeling to show that lithospheric loading in the form of body forces, denudation, and sedimentation all influence current deformation in the Pyrenees.

Extension in high-topography regions is an expected consequence of high GPE, commonly observed in other orogenies worldwide (Flesch & Kreemer, 2010; Levandowski et al., 2017). In Iberia, clusters with normal mid-focal mechanisms (Cluster P in Galicia, Cluster T in the Betics, and Cluster I in the Pyrenees; Figure 5d), as well as several nonclustered normal stress indicators (Iberian Chain and Rif; Figure 5c), coincide with local GPE maxima (Figure 2). In these areas, the GPE stresses fit the observed extensional regimes: the extensional direction from the GPE-derived stress field is parallel to the *T* axis of earthquakes' focal mechanisms and to the extension direction of active normal faults, particularly in the Iberian Chain and in the Eastern Betics (Figure 1; García-Mayordomo, 2012). In these areas, which are typically more than 1,500 m high, the dominant driving force is likely GPE rather than plate boundary forces.

The literature concerning this topic recognizes that GPE is, in general, insufficient to account for the observed deformation. In a global joint model of lithosphere and mantle dynamics, the isolated contribution of the GPE to the total deviatoric stress has been estimated as 50% (Ghosh, Holt, et al., 2013). For North America, GPE has been also estimated to account for 50% of the deviatoric stresses driving deformation, the remaining being due to plate boundary stresses (Flesch et al., 2007). Using a balancing forcing model (net zero torque) for the Eurasia plate, Warners-Ruckstuhl et al. (2013) estimated that GPE (lithospheric body forces) contributes 10%–30% of the total net torque. This compares well with our results, which show that stresses generated by GPE are on average only about 20% of the magnitude of the total stress in Iberia.

The results of this study concerning the relative contribution of gravitational potential energy (GPE model) with respect to other forces (TOTAL model) driving active deformation in Iberia are synthetized in Table 2. The dominant driving mechanism in most of Iberia and its surrounding regions is the Nubia-Eurasia convergence. As shown by Neres et al. (2016), slab-related mechanisms modeled as basal shear traction are also needed in order to match observations in the Alboran domain. In addition, stress localization due to active faults along the plate boundary, particularly in the Gulf of Cadiz, also plays an important role in the TOTAL model. Finally, GPE explains several unexpected stress patterns in terms of direction (deflection from the direction of tectonic convergence) and faulting regime (extensional regimes in a general compressive setting), which are observed at both local (internal Betics, Galicia Massif, Pyrenees, and Rif) and regional (Iberian Chain) scales, always associated with high topography.

The main stress and strain rate patterns in Iberia are characterized by dominant strike-slip (western and central Iberia, western Betics, and Alboran Sea) and thrust faulting regimes (Gulf of Cadiz and Algerian margin), related to the present-day Nubia-Eurasia convergence. In the Alboran domain, more complex stress and strain rate patterns are due to the presence of the subducted slab that is still attached underneath the Gibraltar arc (Mancilla et al., 2013; Neres et al., 2016). Across the Gibraltar arc, an additional source of high GPE is needed in order to explain some of the normal faulting style data of the WSM2016 database and some of the strain rate observations. A contribution to GPE from dynamic topography (vertical components of mantle flow) induced by slab dynamics (e.g., Becker et al., 2015; Faccenna & Becker, 2010; Molnar et al., 2015) could be a plausible hypothesis (as suggested also by Palano et al., 2013) that calls for further investigation.

Coherent folding of both surface and intralithospheric density interfaces, especially during Eocene-lower Miocene times, supports previous studies suggesting that Iberia is folded at the lithospheric scale (Cloetingh et al., 2002). However, the NW-SE to WNW-ESE trend of the Iberian Chain and Pyrenees shows that inherited tectonic fabrics, such as plate boundaries and Mesozoic rift basins, controlled the tectonic inversion patterns and mountain building, in line with the observation that present-day convergence occurs mostly along reactivated inherited tectonic structures (e.g., Ramos et al., 2017; Sallarès et al., 2013).

Table 2
Key Observations and Results From the Analysis of GPE and TOTAL Models Versus Stress and Strain Rate Data

Scale	Geographic subregion	Stress data (fault regime)	Strain rate data (fault regime)	Dominant forcing
Regional	Western and Central Iberia	NW-SE SH_{max} (strike-slip)	Patchy pattern (mostly strike-slip)	NU-EU convergence
	Iberian Chain	NW-SE SH_{max} (normal)	N-S εH_{min} (normal)	GPE
	Gulf of Cadiz	NW-SE SH_{max} (thrust/strike-slip)	NW-SE εH_{min} (thrust/strike-slip)	NU-EU convergence/active faulting
	Valencia Trough	NNE-SSW SH_{max} (strike-slip)	E-W εH_{min} (strike-slip)	NU-EU convergence
	Alboran Sea	NNW-SSE SH_{max} (strike-slip)	NW-SE εH_{min} (strike-slip)	NU-EU convergence/basal traction (subducting slab)
	Algerian margin	NE-SW SH_{max} (thrust)	NW-SE εH_{min} (strike-slip)	NU-EU convergence/active faulting
	Eastern Betics	NW-SE SH_{max} (strike-slip)	NW-SE εH_{min} (strike-slip)	NU-EU convergence/active faulting
Local	Internal Betics/*Cluster T*	NW-SE SH_{max} (normal)	NW-SE εH_{min} (strike-slip)	GPE
	Galicia Massif/*Cluster P*	NW-SE SH_{max} (normal)	Patchy pattern	GPE/model lacks faults
	Pyrenees/*Cluster I*	NNE-SSW SH_{max} (normal)	Patchy pattern	GPE/model lacks faults
	Rif	NNW-SSE SH_{max} (normal)	E-W εH_{min} (strike-slip)	GPE/basal traction

Note. For each relevant geographical area: horizontal stress orientation and regional or local faulting regime inferred from WSM data or midfocal mechanism, orientation of geodetic strain rate and respective dominant faulting regime, and inferred dominant driving force.

The present-day GPE stresses and strain rates, related to high topography and folding, are indirect consequences of past tectonic stresses and strain and reflect their propagation from the plate boundary into the intracontinental region. The similar orientation of SH_{max} for GPE and TOTAL models over a substantial part of continental Iberia, both striking NW-SE, reflects this process. Our study supports previous work that suggests that the main role of GPE in the Iberian Peninsula is to cause spatial variations in the stress regime (Andeweg, 2002; Gölke & Coblentz, 1996; Neves et al., 2014), specifically by inducing extensional regimes in high-topography (>1,500-m) regions. However, it opposes their conclusion that its main effect is to counteract the prevalent NW-SE compression.

8. Conclusions

The stress and strain rate fields in the Iberian lithosphere are largely dominated by the driving effect of tectonic boundary stresses induced by theNubia-Eurasia convergence. Basal shear beneath the westward driven Alboran microplate and fault activity, especially along the plate boundary zone, are also important sources of deformation.

GPE explains unexpected stress patterns, in terms of both direction (deviation of SH_{max} from the direction related to the tectonic convergence) and faulting regime (extensional regimes in a general compressive setting) at local and regional scales, associated with high topography.

Normal faulting regimes in Iberia appear to be associated with GPE maxima. Shallow earthquake clusters with normal mid-focal mechanisms and several nonclustered WSM normal stress indicators coincide with regions where gravitational potential stresses cause extensional regimes.

In central Iberia, the topography and GPE have perfectly matching folding wavelengths of approximately 150 and 350 km, oriented perpendicular to the Nubia-Eurasia direction of convergence during the Eocene-lower Miocene. This indicates coherent folding of both surface and intralithospheric density interfaces during the Pyrenean orogeny.

The present-day GPE-derived stresses and strain rates, related to high topography and folding, are indirect consequences of past tectonics and reflect the propagation of deformation from the plate boundary into the intracontinental region.

Acknowledgments
We acknowledge support by project FCT UID/GEO/50019/2013-Instituto Dom Luiz. M. N. acknowledges support by the Portuguese National Science Foundation (fellowship SFRH/BPD/96829/2013). MMCC research was supported by project MIUR-FIRB "Abruzzo" (code: RBAP10ZC8K_001) and Project L. R. Abruzzo 37/2016 (Indagini di geologia, sismologia e geodesia per la mitigazione del rischio sismico). The GPS solutions were computed using resources provided by C4-Collaboratory for Geosciences (POCI-01-0145-FEDER-022151). The work presented further benefitted from the support of FCT project SPIDER—Seismogenic Processes In slowly DEforming Regions (PTDC/GEO-FIQ/2590/2014). GPE and the stress and strain rate fields were modeled using the code SHELLS.f90 available at http://peterbird.name/oldFTP/neotec/Shells/. The GNSS data set is available as supporting information. WSM data can be accessed at http://www.world-stress-map.org/download/. Figures were prepared with GMT software tools (Wessel et al., 2013). We thank the Editor Paul Tregoning, Will Levandowski, and other three anonymous reviewers for their helpful and constructive comments and suggestions.

References

Amante, C., & C. W. Eakins (2009). ETOPO1 1 Arc-Minute Global Relief Model: Procedures, data sources and analysis NOAA Technical Memorandum NESDIS NGDC-24. National Geophysical Data Center, *NOAA*. https://doi.org/10.7289/V5C8276M

Andeweg, B. (2002). Cenozoic tectonic evolution of the Iberian Peninsula: Effects and causes of changing stress fields, Vrije Universiteit.

Artyushkov, E. (1973). Stresses in the lithosphere caused by crustal thickness inhomogeneities. *Journal of Geophysical Research*, *78*, 7675–7708. https://doi.org/10.1029/JB078i032p07675

Basili, R., Kastelic, V., Demircioglu, M., Garcia Moreno, D., Nemser, E., Petricca, P., et al. (2013). The European Database of Seismogenic Faults (EDSF) compiled in the framework of the Project SHARE. http://diss.rm.ingv.it/share-edsf

Becker, T. W., Lowry, A. R., Faccenna, C., Schmandt, B., Borsa, A., & Yu, C. (2015). Western US intermountain seismicity caused by changes in upper mantle flow. *Nature*, *524*(7566), 458–461. https://doi.org/10.1038/nature14867

Becker, T. W., & O'Connell, R. J. (2001). Predicting plate velocities with mantle circulation models. *Geochemistry, Geophysics, Geosystems*, *2*, 1060–1054. https://doi.org/10.1029/2001GC000171

Bird, P. (1989). New finite element techniques for modeling deformation histories of continents with stratified temperature-dependent rheology. *Journal of Geophysical Research*, *94*, 3967–3990. https://doi.org/10.1029/JB094iB04p03967

Bird, P. (1999). Thin-plate and thin-shell finite-element programs for forward dynamic modeling of plate deformation and faulting. *Computers & Geosciences*, *25*(4), 383–394. https://doi.org/10.1016/S0098-3004(98)00142-3

Bird, P., Liu, Z., & Rucker, W. K. (2008). Stresses that drive the plates from below: Definitions, computational path, model optimization, and error analysis. *Journal of Geophysical Research*, *113*, B11406. https://doi.org/10.1029/2007JB005460

Bird, P., & Piper, K. (1980). Plane-stress finite-element models of tectonic flow in southern California. *Physics of the Earth and Planetary Interiors*, *21*(2–3), 158–175. https://doi.org/10.1016/0031-9201(80)90067-9

Boehm, J., Kouba, J., & Schuh, H. (2009). Forecast Vienna Mapping Functions 1 for real-time analysis of space geodetic observations. *Journal of Geodesy*, *83*(5), 397–401. https://doi.org/10.1007/s00190-008-0216-y

Bos, M., Fernandes, R., Williams, S., & Bastos, L. (2013). Fast error analysis of continuous GNSS observations with missing data. *Journal of Geodesy*, *87*(4), 351–360. https://doi.org/10.1007/s00190-012-0605-0

Bousquet, J. (1979). Quaternary strike-slip faults in southeastern Spain. *Tectonophysics*, *52*(1–4), 277–286. https://doi.org/10.1016/0040-1951(79)90232-4

Buforn, E., De Galdeano, C. S., & Udías, A. (1995). Seismotectonics of the Ibero-Maghrebian region. *Tectonophysics*, *248*(3–4), 247–261. https://doi.org/10.1016/0040-1951(94)00276-F

Cabral, J. (1989). An example of intraplate neotectonic activity, Vilariça basin, Northeast Portugal. *Tectonics*, *8*, 285–303. https://doi.org/10.1029/TC008i002p00285

Cabral, J. (2012). Neotectonics of mainland Portugal: State of the art and future perspectives/Neotectónica de Portugal peninsular—Estado de la cuestión y perspectivas de futuro. *Journal of Iberian Geology*, *38*(1), 71–84.

Camelbeeck, T., de Viron, O., Van Camp, M., & Kusters, D. (2013). Local stress sources in Western Europe lithosphere from geoid anomalies. *Lithosphere*, *5*(3), 235–246. https://doi.org/10.1130/L238.1

Cannavò, F., & Palano, M. (2016). Defining geodetic reference frame using Matlab®: PlatEMotion 2.0. *Pure and Applied Geophysics*, *173*(3), 937–944. https://doi.org/10.1007/s00024-015-1112-z

Carafa, M., & Barba, S. (2011). Determining rheology from deformation data: The case of central Italy. *Tectonics*, *30*, TC2003. https://doi.org/10.1029/2010TC002680

Carafa, M., & Barba, S. (2013). The stress field in Europe: Optimal orientations with confidence limits. *Geophysical Journal International*, *193*(2), 531–548. https://doi.org/10.1093/gji/ggt024

Carafa, M., Barba, S., & Bird, P. (2015). Neotectonics and long-term seismicity in Europe and the Mediterranean region. *Journal of Geophysical Research: Solid Earth*, *120*, 5311–5342. https://doi.org/10.1002/2014JB011751

Carafa, M. M., Tarabusi, G., & Kastelic, V. (2015). SHINE: Web application for determining the horizontal stress orientation. *Computers & Geosciences*, *74*, 39–49. https://doi.org/10.1016/j.cageo.2014.10.001

Casas-Sainz, A., & De Vicente, G. (2009). On the tectonic origin of Iberian topography. *Tectonophysics*, *474*(1-2), 214–235. https://doi.org/10.1016/j.tecto.2009.01.030

Chevrot, S., Villaseñor, A., Sylvander, M., Benahmed, S., Beucler, E., Cougoulat, G., et al. (2014). High-resolution imaging of the Pyrenees and Massif Central from the data of the PYROPE and IBERARRAY portable array deployments. *Journal of Geophysical Research: Solid Earth*, *119*, 6399–6420. https://doi.org/10.1002/2014JB010953

Cloetingh, S., Burov, E., Beekman, F., Andeweg, B., Andriessen, P., Garcia-Castellanos, D., et al. (2002). Lithospheric folding in Iberia. *Tectonics*, *21*(5), 1041. https://doi.org/10.1029/2001TC901031

Cloetingh, S., Thybo, H., & Faccenna, C. (2009). TOPO-EUROPE: Studying continental topography and Deep Earth–Surface processes in 4D. *Tectonophysics*, *474*(1–2). 4–32. https://doi.org/10.1016/j.tecto.2009.04.015

Coblentz, D. D., & Sandiford, M. (1994). Tectonic stresses in the African plate: Constraints on the ambient lithospheric stress state. *Geology*, *22*(9), 831–834. https://doi.org/10.1130/0091-7613(1994)022<0831:TSITAP>2.3.CO;2

Cunha, T., Matias, L., Terrinha, P., Negredo, A., Rosas, F., Fernandes, R., & Pinheiro, L. (2012). Neotectonics of the SW Iberia margin, Gulf of Cadiz and Alboran Sea: A reassessment including recent structural, seismic and geodetic data. *Geophysical Journal International*, *188*(3), 850–872. https://doi.org/10.1111/j.1365-246X.2011.05328.x

Custódio, S., Lima, V., Vales, D., Cesca, S., & Carrilho, F. (2016). Imaging active faulting in a region of distributed deformation from the joint clustering of focal mechanisms and hypocentres: Application to the Azores–western Mediterranean region. *Tectonophysics*, *676*, 70–89. https://doi.org/10.1016/j.tecto.2016.03.013

DeLarouzière, F., Bolze, J., Bordet, P., Hernandez, J., Montenat, C., & d'Estevou, P. O. (1988). The Betic segment of the lithospheric Trans-Alboran shear zone during the Late Miocene. *Tectonophysics*, *152*(1–2), 41–52. https://doi.org/10.1016/0040-1951(88)90028-5

De Vicente, G., & Vegas, R. (2009). Large-scale distributed deformation controlled topography along the western Africa–Eurasia limit: Tectonic constraints. *Tectonophysics*, *474*(1-2), 124–143. https://doi.org/10.1016/j.tecto.2008.11.026

DeMets, C., Gordon, R. G., & Argus, D. F. (2010). Geologically current plate motions. *Geophysical Journal International*, *181*(1), 1–80. https://doi.org/10.1111/j.1365-246X.2009.04491.x

Duarte, J. C., Rosas, F. M., Terrinha, P., Gutscher, M.-A., Malavieille, J., Silva, S., & Matias, L. (2011). Thrust–wrench interference tectonics in the Gulf of Cadiz (Africa–Iberia plate boundary in the north-East Atlantic): Insights from analog models. *Marine Geology*, *289*(1-4), 135–149. https://doi.org/10.1016/j.margeo.2011.09.014

Duarte, J. C., Rosas, F. M., Terrinha, P., Schellart, W. P., Boutelier, D., Gutscher, M.-A., & Ribeiro, A. (2013). Are subduction zones invading the Atlantic? Evidence from the southwest Iberia margin. *Geology*, *41*(8), 839–842. https://doi.org/10.1130/G34100.1

Faccenna, C., & Becker, T. W. (2010). Shaping mobile belts by small-scale convection. *Nature*, *465*(7298), 602–605. https://doi.org/10.1038/nature09064

Farolfi, G., & Del Ventisette, C. (2017). Strain rates in the Alpine Mediterranean region: Insights from advanced techniques of data processing. *GPS Solutions*, *21*(3), 1027–1036. https://doi.org/10.1007/s10291-016-0588-z

Fernandes, R., Ambrosius, B., Noomen, R., Bastos, L., Wortel, M., Spakman, W., & Govers, R. (2003). The relative motion between Africa and Eurasia as derived from ITRF2000 and GPS data. *Geophysical Research Letters*, *30*(16), 1828. https://doi.org/10.1029/2003GL017089

Fleitout, L., & Froidevaux, C. (1982). Tectonics and topography for a lithosphere containing density heterogeneities. *Tectonics*, *1*, 21–56. https://doi.org/10.1029/TC001i001p00021

Flesch, L. M., Holt, W. E., Haines, A. J., Wen, L., & Shen-Tu, B. (2007). The dynamics of western North America: Stress magnitudes and the relative role of gravitational potential energy, plate interaction at the boundary and basal tractions. *Geophysical Journal International*, *169*(3), 866–896. https://doi.org/10.1111/j.1365-246X.2007.03274.x

Flesch, L. M., & Kreemer, C. (2010). Gravitational potential energy and regional stress and strain rate fields for continental plateaus: Examples from the central Andes and Colorado Plateau. *Tectonophysics*, *482*(1–4), 182–192. https://doi.org/10.1016/j.tecto.2009.07.014

García-Mayordomo, J. (2012). The Quaternary Active Faults Database of Iberia (QAFI v. 2.0)/La Base de Datos de Fallas Activas en el Cuaternario de Iberia (QAFI v. 2.0). *Journal of Iberian Geology*, *38*(1), 285–302.

Genti, M., Chery, J., Vernant, P., & Rigo, A. (2016). Impact of gravity forces and topography denudation on normal faulting in Central–Western Pyrenees: Insights from 2D numerical models. *Comptes Rendus Geoscience*, *348*(3-4), 173–183. https://doi.org/10.1016/j.crte.2015.08.004

Ghosh, A., Becker, T., & Humphreys, E. (2013). Dynamics of the North American continent. *Geophysical Journal International*, *194*(2), 651–669. https://doi.org/10.1093/gji/ggt151

Ghosh, A., Holt, W., & Wen, L. (2013). Predicting the lithospheric stress field and plate motions by joint modeling of lithosphere and mantle dynamics. *Journal of Geophysical Research: Solid Earth*, *118*, 346–368. https://doi.org/10.1029/2012JB009516

Ghosh, A., & Holt, W. E. (2012). Plate motions and stresses from global dynamic models. *Science*, *335*(6070), 838–843. https://doi.org/10.1126/science.1214209

Ghosh, A., Holt, W. E., Flesch, L. M., & Haines, A. J. (2006). Gravitational potential energy of the Tibetan Plateau and the forces driving the Indian plate. *Geology*, *34*(5), 321–324. https://doi.org/10.1130/G22071.1

Gölke, M., & Coblentz, D. (1996). Origins of the European regional stress field. *Tectonophysics*, *266*(1–4), 11–24. https://doi.org/10.1016/S0040-1951(96)00180-1

Gutscher, M.-A., Dominguez, S., Westbrook, G. K., LeRoy, P., Rosas, F., Duarte, J., et al. (2012). The Gibraltar subduction: A decade of new geophysical data. *Tectonophysics*, *574*, 72–91.

Hackl, M., Malservisi, R., & Wdowinski, S. (2009). Strain rate patterns from dense GPS networks. *Natural Hazards and Earth System Sciences*, *9*(4), 1177–1187. https://doi.org/10.5194/nhess-9-1177-2009

Heidbach, O., M. Rajabi, M. Ziegler, & K. Reiter (2016). The World Stress Map database release 2016—Global crustal stress pattern vs. absolute plate motion, edited, p. 4861, GFZ data services.

Hodges, K., Hurtado, J., & Whipple, K. (2001). Southward extrusion of Tibetan crust and its effect on Himalayan tectonics. *Tectonics*, *20*, 799–809. https://doi.org/10.1029/2001TC001281

Jones, C. H., Unruh, J. R., & Sonder, L. J. (1996). The role of gravitational potential energy in active deformation in the southwestern United States. *Nature*, *381*(6577), 37–41. https://doi.org/10.1038/381037a0

Kagan, Y. (1991). 3-D rotation of double-couple earthquake sources. *Geophysical Journal International*, *106*(3), 709–716. https://doi.org/10.1111/j.1365-246X.1991.tb06343.x

Kong, X., & Bird, P. (1995). SHELLS: A thin-shell program for modeling neotectonics of regional or global lithosphere with faults. *Journal of Geophysical Research*, *100*, 22,129–22,131. https://doi.org/10.1029/95JB02435

Koulali, A., Ouazar, D., Tahayt, A., King, R., Vernant, P., Reilinger, R., et al. (2011). New GPS constraints on active deformation along the Africa–Iberia plate boundary. *Earth and Planetary Science Letters*, *308*(1-2), 211–217. https://doi.org/10.1016/j.epsl.2011.05.048

Leblanc, D., & Olivier, P. (1984). Role of strike-slip faults in the Betic-Rifian orogeny. *Tectonophysics*, *101*(3–4), 345–355. https://doi.org/10.1016/0040-1951(84)90120-3

Levandowski, W., Zellman, M., & Briggs, R. (2017). Gravitational body forces focus North American intraplate earthquakes. *Nature Communications*, *8*. https://doi.org/10.1038/ncomms14314

Lichten, S., Bar-Sever, Y., Bertiger, E., Heflin, M., Hurst, K., Muellerschoen, R., et al. (2006). GIPSY-OASIS II: A high precision GPS data processing system and general orbit analysis tool. *Technology*, *2*(6), 2–4.

Lithgow-Bertelloni, C., & Richards, M. A. (1998). The dynamics of Cenozoic and Mesozoic plate motions. *Reviews of Geophysics*, *36*, 27–78. https://doi.org/10.1029/97RG02282

Lonergan, L., & White, N. (1997). Origin of the Betic-Rif mountain belt. *Tectonics*, *16*, 504–522. https://doi.org/10.1029/96TC03937

Mancilla, F. d. L., Booth-Rea, G., Stich, D., Pérez-Peña, J. V., Morales, J., Azañón, J. M., et al. (2015). Slab rupture and delamination under the Betics and Rif constrained from receiver functions. *Tectonophysics*, *663*, 225–237. https://doi.org/10.1016/j.tecto.2015.06.028

Mancilla, F. d. L., Stich, D., Berrocoso, M., Martín, R., Morales, J., Fernandez-Ros, A., et al. (2013). Delamination in the Betic Range: Deep structure, seismicity, and GPS motion. *Geology*, *41*(3), 307–310. https://doi.org/10.1130/G33733.1

Martín-González, F., Antón, L., Insua, J., DeVicente, G., Martínez-Díaz, J., Muñoz-Martín, A., et al. (2012). Seismicity and potencially active faults in the northwest and central-west Iberian Peninsula/Sismicidad y Fallas Potencialmente Activas en el Noroeste y Centro Oeste de la Península Ibérica. *Journal of Iberian Geology*, *38*(1), 53.

Molinari, I., & Morelli, A. (2011). EPcrust: A reference crustal model for the European Plate. *Geophysical Journal International*, *185*(1), 352–364. https://doi.org/10.1111/j.1365-246X.2011.04940.x

Molnar, P., England, P. C., & Jones, C. H. (2015). Mantle dynamics, isostasy, and the support of high terrain. *Journal of Geophysical Research: Solid Earth*, *120*, 1932–1957. https://doi.org/10.1002/2014JB011724

Molnar, P., & Lyon-Caen, H. (1988). Some simple physical aspects of the support, structure, and evolution of mountain belts. *Geological Society of America Special Papers*, *218*, 179–208. https://doi.org/10.1130/SPE218-p179

Moucha, R., & Forte, A. M. (2011). Changes in African topography driven by mantle convection. *Nature Geoscience*, *4*(10), 707–712. https://doi.org/10.1038/ngeo1235

Neres, M., Carafa, M., Fernandes, R., Matias, L., Duarte, J., Barba, S., & Terrinha, P. (2016). Lithospheric deformation in the Africa-Iberia plate boundary: Improved neotectonic modeling testing a basal-driven Alboran plate. *Journal of Geophysical Research: Solid Earth*, *121*, 6566–6596. https://doi.org/10.1002/2016JB013012

Neves, M. C., Fernandes, R. M., & Adam, C. (2014). Refined models of gravitational potential energy compared with stress and strain rate patterns in Iberia. *Journal of Geodynamics*, *81*, 91–104. https://doi.org/10.1016/j.jog.2014.07.010

Palano, M., González, P. J., & Fernández, J. (2013). Strain and stress fields along the Gibraltar Orogenic Arc: Constraints on active geodynamics. *Gondwana Research*, *23*(3), 1071–1088. https://doi.org/10.1016/j.gr.2012.05.021

Palano, M., González, P. J., & Fernández, J. (2015). The diffuse plate boundary of Nubia and Iberia in the Western Mediterranean: Crustal deformation evidence for viscous coupling and fragmented lithosphere. *Earth and Planetary Science Letters*, *430*, 439–447. https://doi.org/10.1016/j.epsl.2015.08.040

Palomeras, I., Villaseñor, A., Thurner, S., Levander, A., Gallart, J., & Harnafi, M. (2017). Lithospheric structure of Iberia and Morocco using finite-frequency Rayleigh wave tomography from earthquakes and seismic ambient noise. *Geochemistry, Geophysics, Geosystems*, *18*, 1824–1840. https://doi.org/10.1002/2016GC006657

Pascal, C. (2006). On the role of heat flow, lithosphere thickness and lithosphere density on gravitational potential stresses. *Tectonophysics*, *425*(1-4), 83–99. https://doi.org/10.1016/j.tecto.2006.07.012

Pascal, C., & Cloetingh, S. A. (2009). Gravitational potential stresses and stress field of passive continental margins: Insights from the south-Norway shelf. *Earth and Planetary Science Letters*, *277*(3-4), 464–473. https://doi.org/10.1016/j.epsl.2008.11.014

Ramos, A., Fernández, O., Terrinha, P., & Muñoz, J. A. (2017). Neogene to recent contraction and basin inversion along the Nubia-Iberia boundary in SW Iberia. *Tectonics*, *36*, 257–286. https://doi.org/10.1002/2016TC004262

Ribeiro, A., Cabral, J., Baptista, R., & Matias, L. (1996). Stress pattern in Portugal mainland and the adjacent Atlantic region, West Iberia. *Tectonics*, *15*, 641–659. https://doi.org/10.1029/95TC03683

Rigo, A., Vernant, P., Feigl, K., Goula, X., Khazaradze, G., Talaya, J., et al. (2015). Present-day deformation of the Pyrenees revealed by GPS surveying and earthquake focal mechanisms until 2011. *Geophysical Journal International*, *201*(2), 947–964. https://doi.org/10.1093/gji/ggv052

Ritsema, J., Deuss, A., VanHeijst, H., & Woodhouse, J. (2011). S40RTS: A degree-40 shear-velocity model for the mantle from new Rayleigh wave dispersion, teleseismic traveltime and normal-mode splitting function measurements. *Geophysical Journal International*, *184*(3), 1223–1236. https://doi.org/10.1111/j.1365-246X.2010.04884.x

Rockwell, T., Fonseca, J., Madden, C., Dawson, T., Owen, L. A., Vilanova, S., & Figueiredo, P. (2009). Palaeoseismology of the Vilariça Segment of the Manteigas-Bragança Fault in northeastern Portugal. *Geological Society, London, Special Publications*, *316*(1), 237–258. https://doi.org/10.1144/sp316.15

Rosenbaum, G., Lister, G. S., & Duboz, C. (2002). Relative motions of Africa, Iberia and Europe during Alpine orogeny. *Tectonophysics*, *359*(1-2), 117–129. https://doi.org/10.1016/S0040-1951(02)00442-0

Royden, L. H. (1993). Evolution of retreating subduction boundaries formed during continental collision. *Tectonics*, *12*, 629–638. https://doi.org/10.1029/92TC02641

Rubey, M., Brune, S., Heine, C., Davies, D. R., Williams, S. E., & Müller, R. D. (2017). Global patterns in Earth's dynamic topography since the Jurassic: The role of subducted slabs. *Solid Earth*, *8*(5), 899–919. https://doi.org/10.5194/se-8-899-2017

Sallarès, V., Martínez-Loriente, S., Prada, M., Gràcia, E., Ranero, C., Gutscher, M.-A., et al. (2013). Seismic evidence of exhumed mantle rock basement at the Gorringe Bank and the adjacent Horseshoe and Tagus abyssal plains (SW Iberia). *Earth and Planetary Science Letters*, *365*, 120–131. https://doi.org/10.1016/j.epsl.2013.01.021

Schmid, R., Dach, R., Collilieux, X., Jäggi, A., Schmitz, M., & Dilssner, F. (2016). Absolute IGS antenna phase center model igs08. atx: Status and potential improvements. *Journal of Geodesy*, *90*(4), 343–364. https://doi.org/10.1007/s00190-015-0876-3

Silva, S., Terrinha, P., Matias, L., Duarte, J. C., Roque, C., Ranero, C. R., et al. (2017). Micro-seismicity in the Gulf of Cadiz: Is there a link between micro-seismicity, high magnitude earthquakes and active faults? *Tectonophysics*, *717*, 226–241. https://doi.org/10.1016/j.tecto.2017.07.026

Smith, W., & Wessel, P. (1990). Gridding with continuous curvature splines in tension. *Geophysics*, *55*(3), 293–305. https://doi.org/10.1190/1.1442837

Spakman, W., & Wortel, R. (2004). A tomographic view on western Mediterranean geodynamics. In *The TRANSMED Atlas: The Mediterranean region from crust to mantle*, (pp. 31–52). https://doi.org/10.1007/978-3-642-18919-7_2

Stamps, D. S., Flesch, L. M., Calais, E., & Ghosh, A. (2014). Current kinematics and dynamics of Africa and the East African Rift System. *Journal of Geophysical Research: Solid Earth*, *119*, 5161–5186. https://doi.org/10.1002/2013JB010717

Stamps, D. S., Iaffaldano, G., & Calais, E. (2015). Role of mantle flow in Nubia-Somalia plate divergence. *Geophysical Research Letters*, *42*, 290–296. https://doi.org/10.1002/2014GL062515

Stich, D., Martín, R., & Morales, J. (2010). Moment tensor inversion for Iberia–Maghreb earthquakes 2005–2008. *Tectonophysics*, *483*(3-4), 390–398. https://doi.org/10.1016/j.tecto.2009.11.006

Stich, D., Serpelloni, E., de Lis Mancilla, F., & Morales, J. (2006). Kinematics of the Iberia–Maghreb plate contact from seismic moment tensors and GPS observations. *Tectonophysics*, *426*(3-4), 295–317. https://doi.org/10.1016/j.tecto.2006.08.004

Terrinha, P., Matias, L., Vicente, J., Duarte, J., Luís, J., Pinheiro, L., et al. (2009). Morphotectonics and strain partitioning at the Iberia–Africa plate boundary from multibeam and seismic reflection data. *Marine Geology*, *267*(3-4), 156–174. https://doi.org/10.1016/j.margeo.2009.09.012

Terrinha, P., Pinheiro, L. M., Henriet, J.-P., Matias, L., Ivanov, M., Monteiro, J. H., et al. (2003). Tsunamigenic-seismogenic structures, neotectonics, sedimentary processes and slope instability on the southwest Portuguese Margin. *Marine Geology*, *195*(1-4), 55–73. https://doi.org/10.1016/S0025-3227(02)00682-5

Vautard, R., Yiou, P., & Ghil, M. (1992). Singular-spectrum analysis: A toolkit for short, noisy chaotic signals. *Physica D: Nonlinear Phenomena*, *58*(1-4), 95–126. https://doi.org/10.1016/0167-2789(92)90103-T

Villaseñor, A., Chevrot, S., Harnafi, M., Gallart, J., Pazos, A., Serrano, I., et al. (2015). Subduction and volcanism in the Iberia–North Africa collision zone from tomographic images of the upper mantle. *Tectonophysics*, *663*, 238–249. https://doi.org/10.1016/j.tecto.2015.08.042

Warners-Ruckstuhl, K. N., Govers, R., & Wortel, R. (2013). Tethyan collision forces and the stress field of the Eurasian Plate. *Geophysical Journal International*, *195*(1), 1–15. https://doi.org/10.1093/gji/ggt219

Wessel, P., & Bercovici, D. (1998). Interpolation with splines in tension: A Green's function approach. *Mathematical Geology*, *30*(1), 77–93. https://doi.org/10.1023/A:1021713421882

Wessel, P., Smith, W. H., Scharroo, R., Luis, J., & Wobbe, F. (2013). Generic mapping tools: Improved version released. *Eos, Transactions American Geophysical Union*, *94*(45), 409–410. https://doi.org/10.1002/2013EO450001

Zitellini, N., Gràcia, E., Matias, L., Terrinha, P., Abreu, M., DeAlteriis, G., et al. (2009). The quest for the Africa–Eurasia plate boundary west of the Strait of Gibraltar. *Earth and Planetary Science Letters*, *280*(1-4), 13–50. https://doi.org/10.1016/j.epsl.2008.12.005

Zumberge, J., Heflin, M., Jefferson, D., Watkins, M., & Webb, F. H. (1997). Precise point positioning for the efficient and robust analysis of GPS data from large networks. *Journal of Geophysical Research*, *102*, 5005–5017. https://doi.org/10.1029/96JB03860